Monte Carlo Multiscale Modelling of Photon and Proton Distributions in Heterogenous Tissue

Ahmad Abbas [1], Richard Hugtenburg [2]

(1) Nuclear Medicine, Ministry of Health, Farwaniya Hospital, Kuwait
(2) Medical Physics, Swansea University Medical School, SA2 8QA, United Kingdom and Singleton Hospital, Swansea Bay University Health Board, Swansea SA2 8QA, United Kingdom

Abstract

Enhancements in radiotherapy treatment outcomes can be realised by minimising uncertainties in dose distribution. Current treatment planning struggles to accurately calculate dose distribution in complex heterogeneous areas, thereby increasing the uncertainty associated with dose distribution. This research focuses on studying microscopic dose distribution in the temporal bone and cochlea. This study utilised an open-access DICOM format dataset for resected temporal bone and cochlea tissue, employing the FLUKA MC code to simulate potential high-dose scenarios in volume-modulated arc therapy using the FLOOD option. Simulations were conducted at 23 photon and proton energy levels, ranging from 0.055 to 5.5 MeV for photons and 37.59 to 124.83 MeV for protons, to calculate dose distributions. The largest proportion of the dose (48.8%) was deposited in high-density bone at photon energies between 0.055 and 0.09 MeV. Above 0.125 MeV, a notable shift in dose distribution to low-density tissues occurred, reaching a deposition of 53%. In intermediate-density soft bone, dose distribution was 26.4% at 0.07 MeV and decreased to 19.7% at 2.5 MeV, reflecting a 29% difference in dose distribution across the energy spectrum. In proton simulations, dose distribution at low energy (37.59 MeV) revealed no significant changes across low (54.86%), intermediate (19.75%), and high-density (25.39%) areas. Similar patterns were observed at high energy (124.83 MeV), with dose distributions of 54.21% in low-, 19.79% in intermediate-, and 26% in high-density areas. The simulations demonstrated that proton dose distribution was not significantly influenced by tissue heterogeneity in micro-CT data. The photoelectric effect at low energy levels contributed minimally to the dose in soft bone, favouring higher deposition in high-density bone, despite a lower weighting factor at low energies compared with high energies.

Keywords: Temporal Bone, Cochlea, Micro-CT data, Monte Carlo, Dose distribution.

1. Introduction

Radiotherapy, administered alone or in conjunction with chemotherapy, is crucial in treating patients with head, neck, or brain tumours. These regions are among the most heterogeneous in the body and encompass numerous organs at risk (OAR) of injury during treatment. Injuries to these areas can significantly impact a patient's quality of life, particularly affecting sensory inputs and normal brain functions such as hearing, vision, and hippocampal function. Increasing the dose to OARs can deteriorate the patient's quality of life and enhance the side effects of radiotherapy. Therefore, selecting the optimal treatment settings in the treatment planning system (TPS), such as dose to water or dose to medium, is critical for optimising treatment outcomes. Moreover, understanding photon behaviour in heterogeneous areas is crucial to reducing dosage delivery errors to the target. However, due to the limited resolution of clinical computed tomography (CT) scans, many details of heterogeneous anatomical areas remain obscured, only observable in higher-resolution CTs such as Micro CT. Numerous studies have shown that in areas with low heterogeneities, the difference between dose to medium and dose to water is typically less than 2%, a margin considered clinically insignificant (Barrett & Keat, 2004; B. Lee et al., 2022; H. Lee et al., 2019). In contrast, in regions containing different densities, particularly those with bone material and air, this difference can reach up to 10% (Barrett & Keat, 2004; B. Lee et al., 2022; H. Lee et al., 2019). This variance arises from differences in interaction cross-sections due to the material compositions of the media, observable at a macroscopic level in mass attenuation, energy absorption coefficients, and electron stopping power (Kry et al., 2020).found significant differences in dose distributions between dose to water and dose to medium, particularly in the cochlea and mandible. Their study revealed that using dose to medium resulted in a lower dose to the cochlea; the cochlea, encased by a bone labyrinth, and the mandible, composed of bones, demonstrated notable differences in dose distribution. Furthermore, Accuros XB reported that dose to medium produced approximately 10% and 13% higher doses in the cochlea and mandible, respectively, compared with dose to water calculations in the same TPS (Muñoz-Montplet et al., 2018). Monte Carlo simulations with general-purpose MC codes are instrumental in reducing dose uncertainty to normal tissues by incorporating a broader range of materials than those derived from clinical CT scans.This study presents a novel MC simulation approach using a patient's Micro CT DICOM series to investigate dose effects in the complex temporal bone area. This method surpasses the limitations of clinical CT and provides a comprehensive analysis of dose distribution, thereby facilitating a more accurate comparison between dose to water and dose to medium in treating the temporal bone and cochlea.

2. Materials and Methods

2.1. Cochlea and temporal bone Micro CT

The study employed an open-access DICOM series from a Micro CT scan of the resected cochlea tissue within the temporal bone, accessible for both research and commercial purposes with appropriate attribution. The data originated from the OpenEar library, which documents its generation process. The temporal bone specimen was prepared by immersing it in phosphate-buffered saline and embedding it in epoxy, with an addition of 0.1% Acid Fuchsin to enhance the contrast. Micro CT images, with a voxel size of 0.125 mm, were reconstructed and registered using the open-source software 3D Slicer version 5.0.2. The registration process involved aligning the Micro CT images with a cone beam, analogous to CT scans.

2.2. Handling Micro CT DICOM using MATLAB

The Hounsfield Unit (HU) scale, which quantifies CT radiodensity, assigns air a value of -1000 HU (appearing black) and dense bone +2000 HU (appearing white). Unlike medical CT scans, Micro CT does not inherently associate voxel values with HU. To overcome this, voxel values from Micro CT are transformed from grayscale to HU using a linear transformation equation, given that X-ray attenuation coefficients correlate directly with grayscale values.

In medical CT, the slope and intercept values facilitating this conversion are typically included in the DICOM header. However, the DICOM series used in this simulation lacked these details. Therefore, these parameters were calculated using MATLAB. The initial step involved uploading the DICOM series into MATLAB, which allowed for the manipulation of the DICOM data. A histogram of voxel values was subsequently generated to identify peaks representing the most frequent grayscale values, which appeared at -538, 709, and 2974. Analysis of these values in relation to their voxel locations indicated that -538 corresponded to air, 709 to soft tissue, and 2974 to bone. Despite the extraction of air in preparing the Micro CT sample, air was detected in the MATLAB analysis.

Only these specific points were plotted and fitted with a linear transformation equation because the study focused on heterogeneity, and these points accurately represented it. Notably, the value for soft tissue was similar to water in medical CT, which was crucial for this study. A visualisation test was subsequently conducted to confirm the accuracy of the imported numbers and to verify the absence of errors.

Moreover, the Micro CT's DICOM data lacked crucial header information necessary for simulations, such as slice location and series number. To rectify this, MATLAB code was employed to insert the missing information while maintaining the DICOM sequence and slice locations. This adjustment included defining slice spacing at 0.125 mm, calculating slice locations, and adding essential header data such as pixel spacing, rescale slope, and acquisition number. After comprehensive validation to

ensure the data was formatted correctly, the Micro CT data was deemed ready for seamless integration into MC simulation code, thereby enhancing its utility in radiotherapy planning and associated applications.

2.3.MC Simulation using FLUKA

In this study, the FLUKA version 4-0 MC simulation engine was utilised along with the FLAIR version 3.0 interface to create geometric shapes. Basic input cards were tailored to integrate DICOM series data into the simulation environment. FLUKA enables the allocation of provisional memory spaces for geometry-dependent arrays prior to determining the exact dimensions, which are reclaimed after input processing concludes. However, when handling an extensive number of regions, specifically over 1000, the program needs to be prompted to expand these provisional memory spaces. This expansion was facilitated using a "GLOBAL" card to support a large number of simulated regions, particularly pertinent when incorporating DICOM data.

Two critical files, "material.inp" and "head.mat," were instrumental in generating the voxel card; the latter contained conversion data crucial for mapping DICOM materials, while the former included material compound cards. Once these files were loaded, FLAIR was able to produce voxel region numbers and organs, and a USBIN to encompass all the voxels. The input card utilised two USBINs: one for recording energy and another for dose. To aid the simulation, a water phantom was created, and the Micro CT data was embedded within this phantom.

The BEAMPOS card was employed to adjust the beam's position, and the FLOOD option was activated to ensure uniform fluence across the target area. The simulation spanned energies from 0.0175 MeV to 5.5 MeV, based on fluence data from preceding studies. An EMFCUT card was utilised to regulate the energy level of electrons within the simulation. Runs involving electrons below 10 KeV and above 11 MeV were excluded to enhance simulation efficiency.

The simulation was conducted in multiple runs, each consisting of five cycles, aiming to reduce statistical uncertainty to below 2%. The FLOOD option was again used to achieve a uniform distribution within the beam's radius, and a uniformity test was conducted to confirm that this uniformity remained within acceptable limits. Overall, this detailed methodology enabled precise simulations pertinent to radiotherapy planning and effectively minimised statistical uncertainty, aligning with the study's objectives.

3. Results

In recent years, the demand for highly accurate radiotherapy treatments has surged, driven by advancements in treatment techniques and treatment planning systems (TPS). These modern TPSs can

utilise Monte Carlo (MC) codes to calculate dose to medium, rather than dose to water, sparking a debate about the optimal mode for their application. A significant question posed by these techniques, particularly in heterogeneous regions with micro-CT data, concerns whether interactions at varying energy levels differ significantly from those observed with current medical CT resolutions, potentially necessitating corrections.

In this study, MC simulations provided exceptional accuracy, albeit at the cost of extended simulation times. Achieving a low percentage of uncertainty was critical to ensure the data was free from significant statistical errors, with all simulations in the project attaining an uncertainty of less than 2%, and a total uncertainty of less than 1%. Such precision was essential to eliminate any potential impact of statistical error on the dose-volume histogram (DVH), an essential tool in radiotherapy planning.

To validate the uniformity of the dose distribution within the target, a series of uniformity tests were conducted. These tests involved processing test files in MATLAB, where a quadratic polynomial was fitted to assess uniformity by examining a line taken from the middle in various directions. The results, depicted in Figure 1, demonstrated a cross-section with a polynomial curve fit, with data points collected from the centre and edges. These tests were performed for simulations both with and without electrons. The polynomial equation indicated that the uniformity was approximately 99% in both scenarios, signifying a highly uniform dose distribution within the target area.

This uniform dose distribution was crucial in accurately replicating the volumetric modulated arc therapy (VMAT) distribution within the target area, highlighting the study's commitment to achieving high precision in radiotherapy planning.

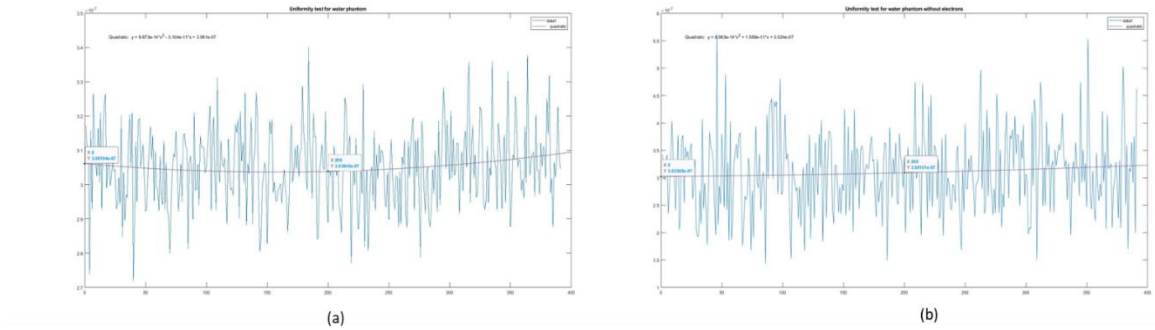

Figure 1: Plot of a cross-section of the water phantom with quadratic polynomials fit: (a) cross-section of simulation with electron interaction, (b) cross-section of simulation without electron interaction.

Following the successful uniformity tests, the next phase of the study involved processing the simulation data in MATLAB. Each energy data set was multiplied by a weighting factor to determine

its contribution to the total beam energy in a treatment scenario. The weighting factor was calculated based on energy distribution data in water, as cited from Yin et al. (2002).

In parallel, a density histogram of the DICOM series Micro CT data was generated, as illustrated in Figure 2. This histogram identified three distinct density regions. The highest peak, spanning the range from 0 to 1.25 g/cm³, corresponded to normal tissue (with a density of 1 g/cm³ being equivalent to water). The second peak, beginning at densities greater than 1.75 g/cm³, indicated the presence of high-density materials such as compact bone. The third density range, from 1.25 to 1.75 g/cm³, emerged from the micro-CT data and represented soft bone.

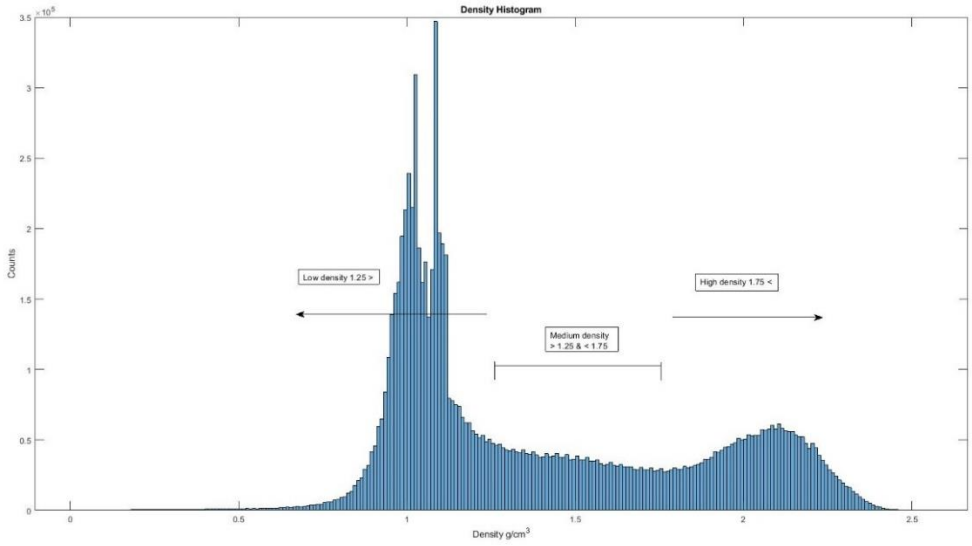

Figure 2: Histogram of the density of the DICOM series.

3.1 Individual Beam Energy

In the prior discussion, simulations were conducted at various energy levels under two different scenarios: one incorporating electrons and the other excluding them. Initially, each energy level was evaluated independently to observe its behaviour within the heterogeneous micro-CT environment. A distinctive pattern was noted across the 23 selected energy levels, indicating variations in their interaction within the Micro CT dataset across three field sizes: 10 × 10, 20 × 20, and 30 × 30 cm.

At energy levels as low as 0.025 MeV, the highest energy deposition was observed in high-density regions, followed by medium-density areas. This deposition pattern was consistent until the beam energy reached 0.07 MeV, at which point a notable shift occurred. The area receiving the highest energy deposition transitioned to high-density regions, while low-density areas became the second most deposited regions.

Another shift in the deposition pattern occurred at a beam energy of 0.125 MeV, where low-density regions received the highest dose deposition ratio, followed by high-density regions, and then medium-density areas. Beyond 0.45 MeV, the dose deposition ratio became more uniform across the densities, with the majority of the dose deposited in soft tissue. For instance, at an energy of 2.5 MeV, the dose deposition ratio was 55.2% for low-density, 19.66% for medium-density, and 25% for high-density areas.

Table 1 provides a detailed breakdown of the changes in ratio levels among different density regions, effectively illustrating the dynamic behaviour of energy deposition as the beam energy increases.

Table 1: Dose distribution at different energy levels.

Energy (MeV)	Low density	Medium density	High density
0.055	23.6%	27.7%	48.8%
0.07	27.4%	26.4%	46.2%
0.09	33.8%	24.7%	41.6%
0.125	43.0%	22.4%	34.6%
0.25	52.8%	20.2%	27.1%
2.5	55.3%	19.7%	25.1%

Figure 3 elucidates the behaviour of individual beams' energy and their interactions with the three density levels: low, medium, and high. At a lower energy of 0.045 MeV, the dose counts were highest in high-density materials (49.26%), compared to low-density (22.2%) and medium-density (28.3%) regions. The dose distribution exhibited a clear separation between low-density and high-density deposition, with a peak dose in soft tissue at $1e^{-10}$ and in bone at $4.8e^{-10}$. This pattern was primarily attributed to the dominance of the photoelectric effect within this energy range. In the low energy range, as shown in Table 1, the highest dose deposition occurs in high-density material; this trend begins to diminish starting at 0.125 MeV energy.

As the energy increased to 0.07 MeV, the dose distribution peaks began to adopt a more Gaussian shape, yet maintained a distribution trend similar to lower energies. By the 0.09 MeV beam, a noticeable shift in dose deposition occurred, with increased dose counts in low-density regions (33.8%) and reductions in medium-density (24.65%) and high-density (41.55%) regions. This trend continued as beam energy increased, favouring greater dose deposits in soft tissue. The difference in dose distribution between low-density and high-density bone reached nearly 50%, primarily influenced by the presence of high atomic number (Z) materials, as detailed in Figure 3(b).

At 0.125 MeV, the dose deposition favoured low-density (42.9%) and high-density (34.59%) regions. At higher energies, individual beams exhibited dose distribution shapes comparable to the cumulative beam output.

Regarding the 2.5 MeV photon beam, the dose distribution demonstrated a significant shift, depositing less dose in high-Z materials compared to low-density materials—a difference of approximately 10%, attributed to the dominant Compton interaction at this energy level, which relies on electron density.

The study noted variations in the percentage change in dose deposition across different energy levels and density materials: soft bone showed the smallest change, with a 26.9% difference between 0.055 MeV and 2.5 MeV. In contrast, hard bone and soft tissue displayed changes of 48.28% and 54.87%, respectively. These findings highlight the intricate interplay between beam energy, material density, and interaction mechanisms—key factors in optimizing radiotherapy planning and dose distribution.

While this study did not calculate the weighting factor as a function of the interaction processes, the photoelectric process accounts for approximately 50% of the energy deposition below 50 keV in soft tissue, whereas this figure demonstrates 150 keV in cortical bone, becoming increasingly dominant at lower energies (‘X-Ray Mass Attenuation Coefficients’, 2009).

(a)

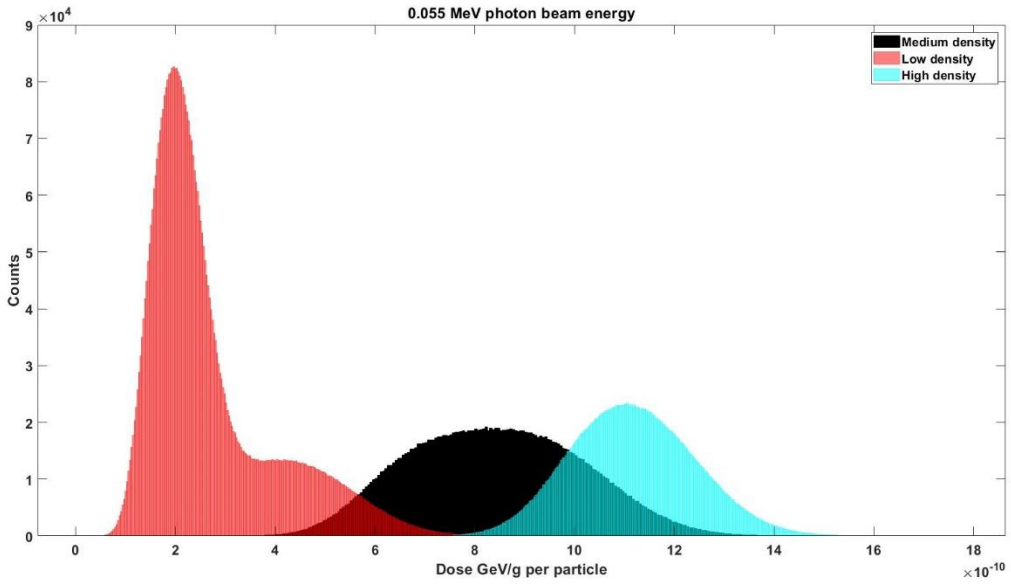

(b)

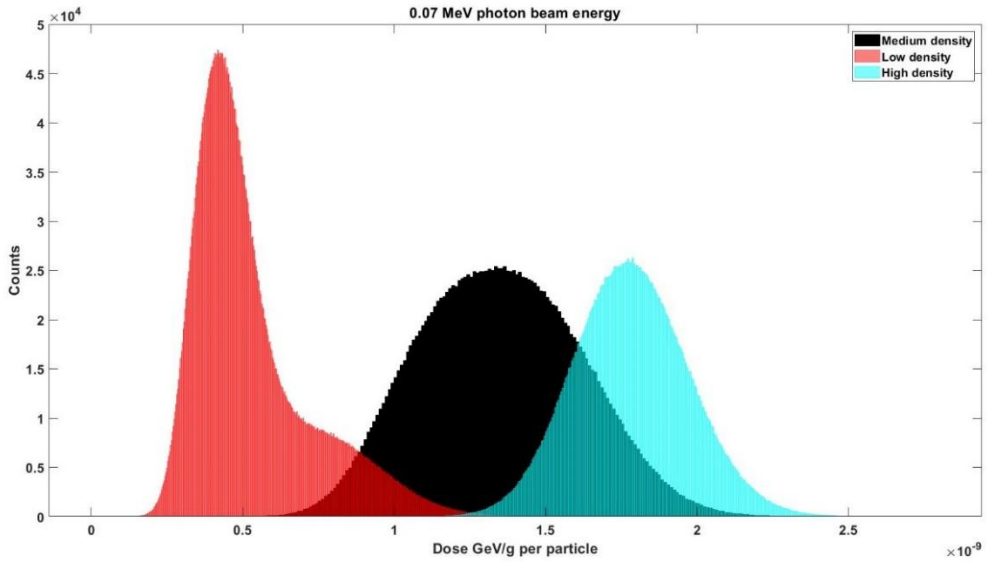
0.07 MeV photon beam energy
Medium density
Low density
High density
Counts
Dose GeV/g per particle
×10^4
×10^-9

(c)

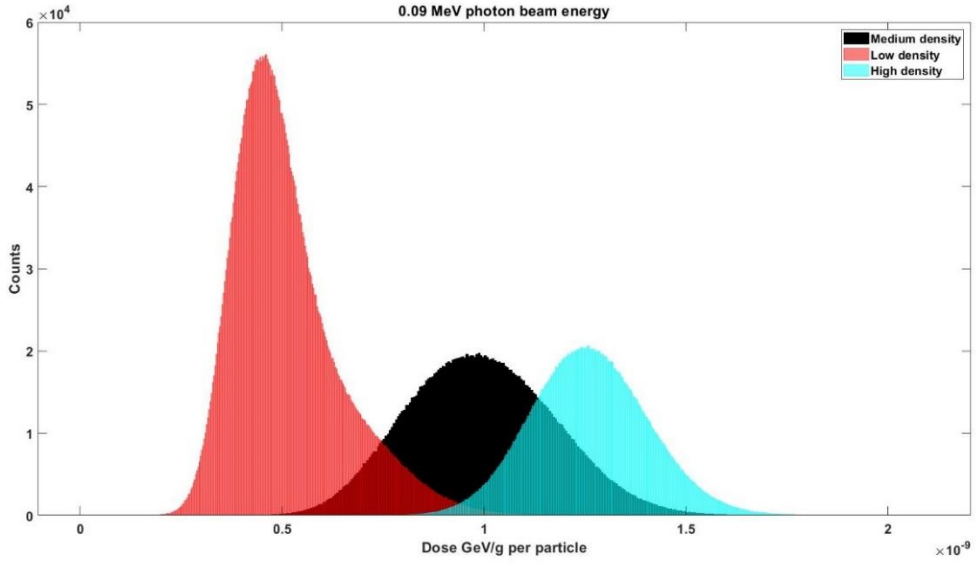
0.09 MeV photon beam energy
Medium density
Low density
High density
Counts
Dose GeV/g per particle
×10^4
×10^-9

(d)

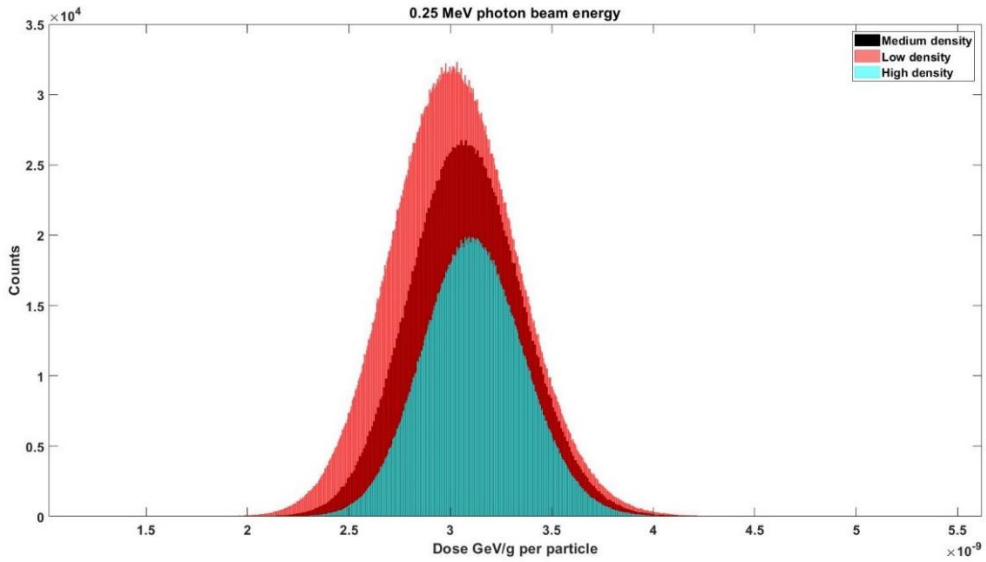

(e)

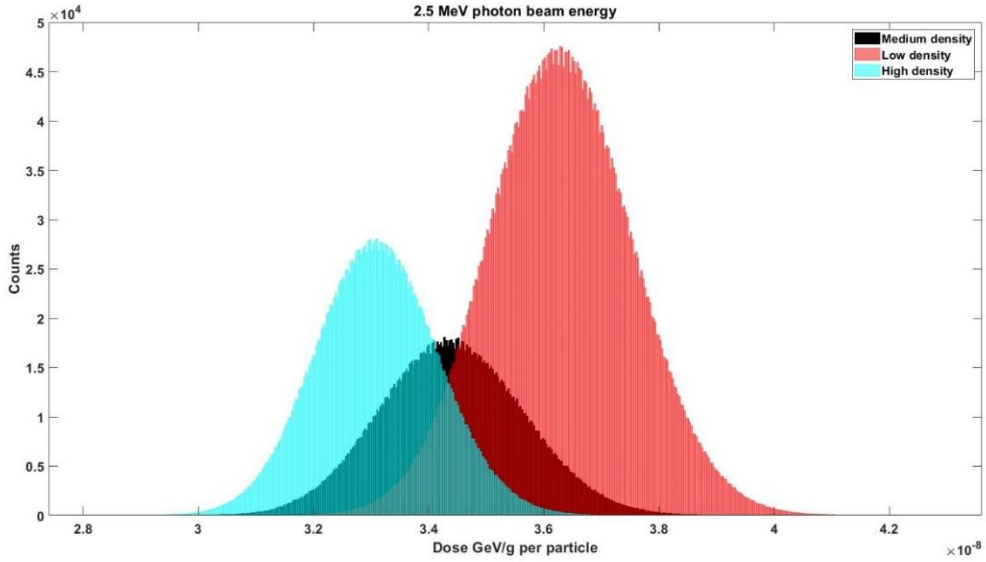

Figure 3: Different dose volume distribution levels in the Micro CT heterogenous area: (a) 0.055 MeV photon energy, (b) 0.07 MeV photon energy, (c) 0.09 MeV photon energy, (d) 0.25 MeV photon energy, and (e) 2.5 MeV photon energy.

3.2 Beam Summation

Assessing individual energy levels is crucial for understanding dose deposition in heterogeneous areas, providing key insights into the behaviour of radiation beams. Moreover, understanding the combined behaviour of energy levels is essential for clinical applications.

Figure 4(a) displays the summation of all simulated beam energies across both scenarios, delineating the separation of the three density levels. Figure 4(b) illustrates the final sum of all simulated beam energies without electron overlaps, covering a dose range from $1.7e^{-7}$ to $2.9e^{-7}$ GeV/g for low-density tissue.

Low-density tissue exhibited the broadest dose range among the three densities, with a dose range of 1.8e-7 to 2.6e-7 GeV/g for high-density tissue. Despite the majority of primary doses being deposited in low-density tissue, a significant proportion of the dose counts were found in high-density regions. In contrast, the medium-density tissue received the lowest dose in simulations that exclusively involved primary photons and excluded electrons.Figure 4(b) displays the summation of beam energies with electrons, emphasising the distinct patterns of energy deposition across the three density ranges without overlap. The inclusion of electrons notably increased the dose counts in low-density areas and decreased them in high-density areas. However, changes in medium-density counts were minimal with the addition of electrons. The shift in peak values at the top of the high- and low-density curves highlighted the impact of electron transport in a heterogeneous environment. The difference in dose distribution between low-density and high-density regions was approximately 10%, mirroring the behaviour observed in the single beam scenario at 2.5 MeV. In high-energy scenarios, the deposition pattern remained relatively consistent due to the dominant Compton interaction in this energy range.

These findings underline the complex interplay of factors influencing dose deposition, including beam energy, material density, and the effects of electron transport. These elements are critical for clinical radiotherapy planning and optimising treatment outcomes, illustrating the necessity of comprehensive simulations to accurately predict and enhance therapeutic efficacy in radiotherapy.

(a)

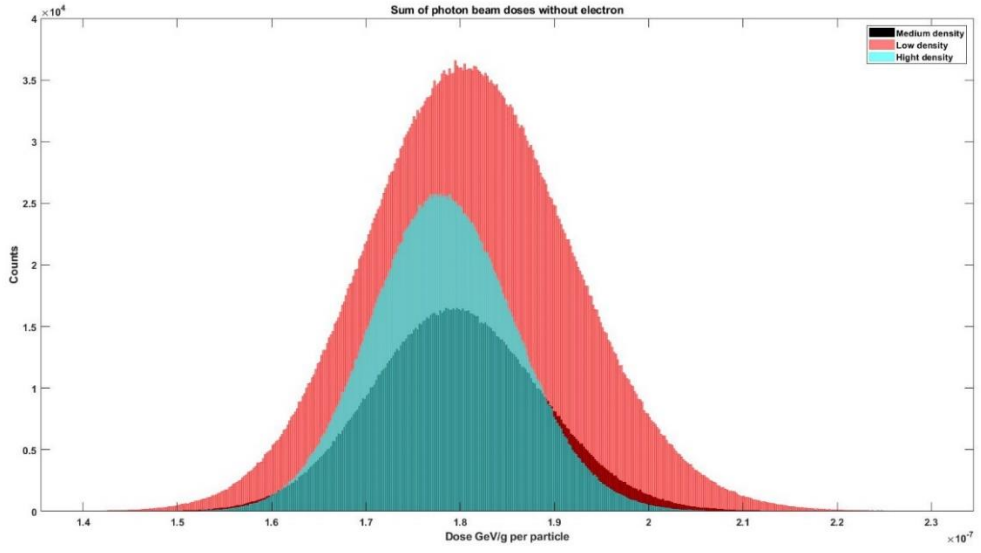

(b)

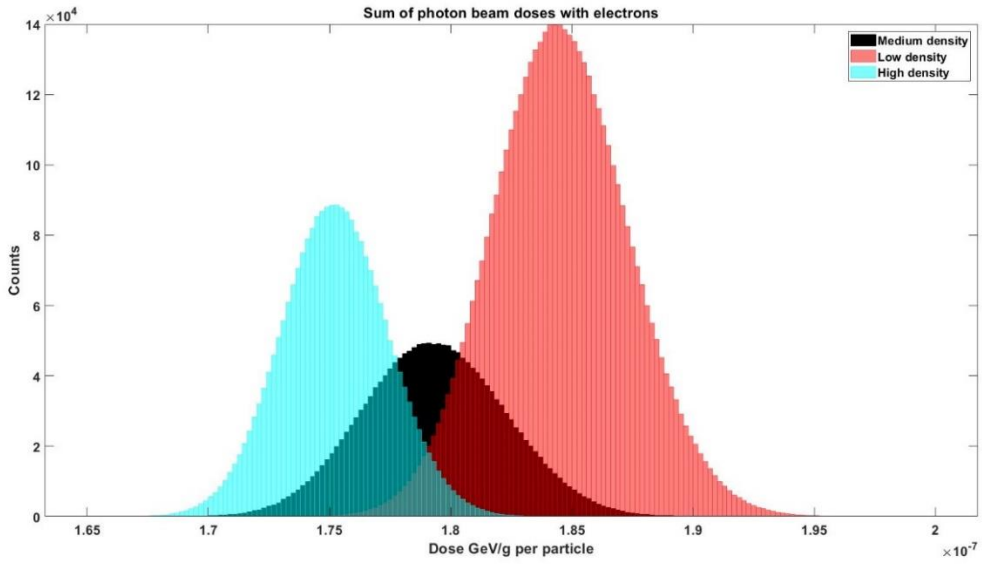

Figure 4: Sum of the photon beam energies, with three divisions of density levels, (a) including the sum of the photon beam with and without electrons (b).

4. Implementing Multiscale Analysis in Clinical Routine

The advanced model developed, based on the dose distribution results from Micro CT scans, comprised two main components. The first part, referred to as the primary, spanned approximately one-third of the arc, as depicted in Figure 5. The field size utilised for this segment was 10×10 cm² at a depth of 1.5 cm. The edge of the arc encompassed two-thirds of the beam, with the distance to the target set at 15 cm. These two principal parts were instrumental in accounting for both primary and scatter radiation events impacting the cochlea.

To derive a practical application of this model in a clinical setting, it was necessary to extract a formula to calculate the weighting factor for determining the dose to the cochlea. The fluence data from a study by Yin *et al.* was employed for calculating this weighted factor (Yin et al., 2002). The first step involved calculating the fluence for the model for each case separately using the following equation:

$$\frac{1}{3}(A)_{1.5cm} + \frac{2}{3}(B - C)_{15cm},$$

where A is the primary beam, with a field size of 10×10 cm^2 at a depth of 1.5 cm. B is the distance from the target to the arc at a depth of 15 cm. C is the distance between the target and cochlea, at a depth of 15 cm. The data utilised from the Cancer Imaging Archive was instrumental in applying the advanced model to various clinical scenarios.

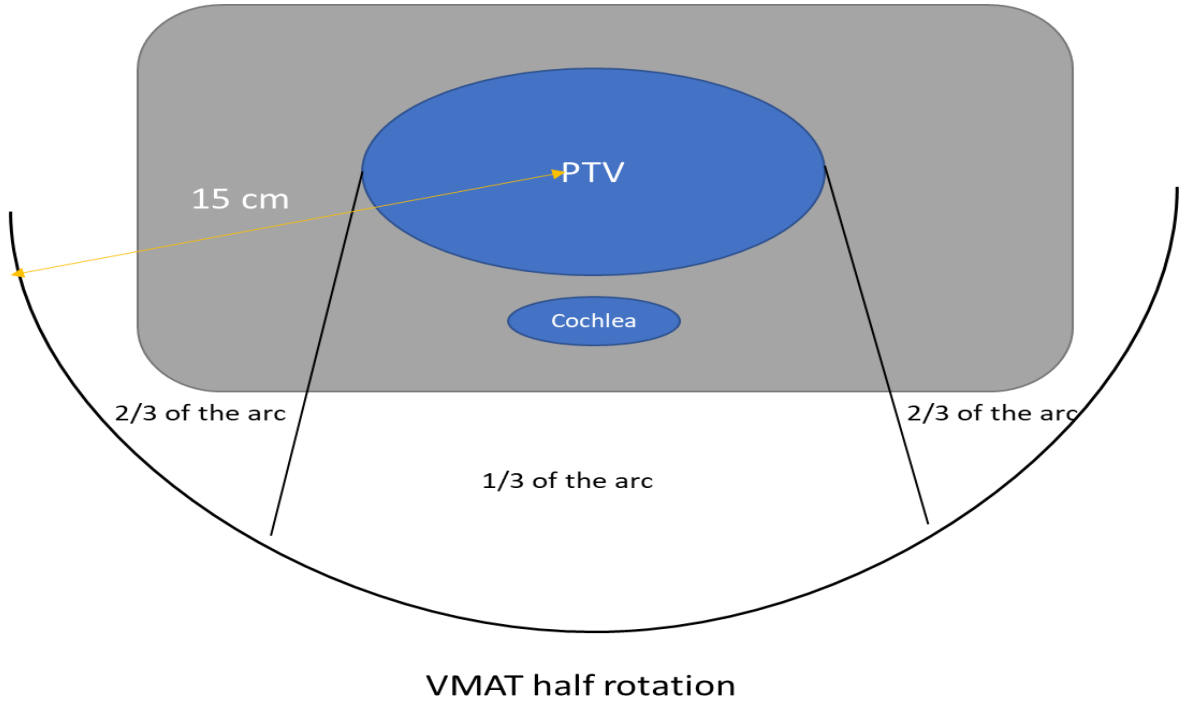

Figure 5: Advanced model used to connect the Monte Carlo result with daily clinical routine.

A DVH comparison could not be conducted without creating a treatment plan for each case. The protocol from a Southwest Wales cancer centre was employed as the dose constraint in each case; the same protocol was used for all treatment plans at the centre. A coplanar arc was selected for all cases under this dose constraint. An Eclipse system, utilising an AAA, was used to generate all plans. A DVH from a TPS was produced and converted into a text format compatible with MATLAB. The final step in processing the data involved creating and comparing both DVHs, which was challenging due to the different scales of the DVHs. The plan was to rescale the MC result and then apply the convolution theorem to combine both datasets.

In the glioma case, where the distance between the target and the cochlea was less than 1 cm, a significant difference was observed in the mean dose, as illustrated in Figure 6. The difference in mean dose was 8%, which was significant. The minimum dose difference reached 10.3% between the two algorithms, and the maximum dose exceeded the clinical constraint to the cochlea in both algorithms. Given the proximity of the cochlea to the target, the plan required re-evaluation to determine if the dose could be reduced without compromising the target dose.

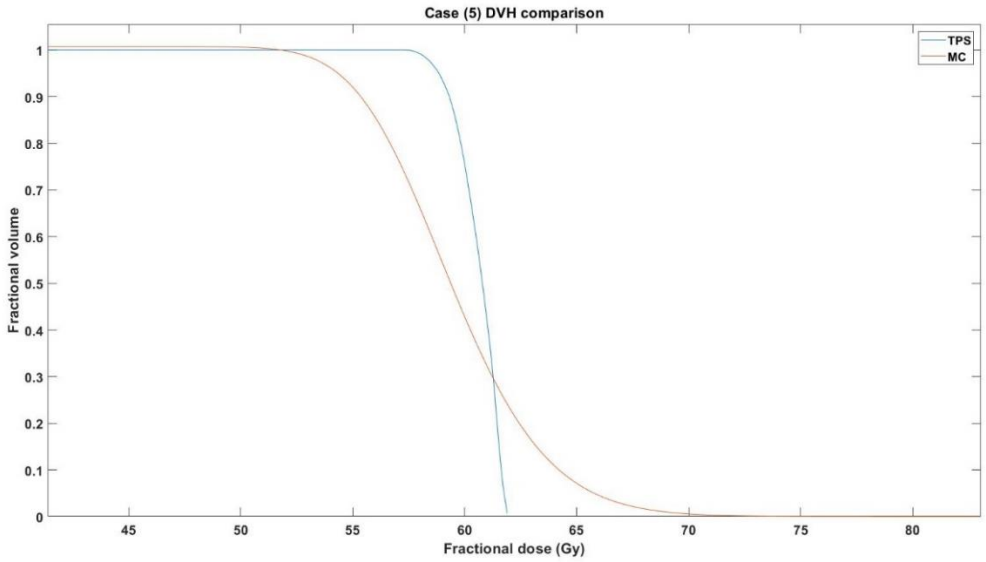

Figure 6: DVH comparison between TPS and Monte Carlo using Micro-CT data.

5. Discussion

Medical CT categorises the temporal bone area as hard bone, soft tissue, and air, as demonstrated in the study by Radojčić et al. (2018). However, clinical CT resolution lacks the anatomical details necessary to detect soft bone, which is not visible at this resolution. Micro CT provides a higher resolution, distinguishing between cortical bone and soft bone, which contains radiation-sensitive red marrow cells (Green & Rubin, 2014). A limitation of Micro CT for the temporal bone is its inability to image air due to the injection of a gel with water-like density, although a small area within the DICOM that contains air is used in calculating the HU scale. In low-level energy interactions, the photoelectric effect predominates. In this study, the increased dose in high and medium density areas, considered bone material, may have resulted from the photoelectric effect, which intensifies with higher density materials. The high heterogeneity and irregular shape of soft and hard bone increase dose deposition at the edges, particularly in high-density areas. However, the contribution of low-level energy to the total beam was minor compared with higher energy levels, and the build-up factor at low energy levels was negligible. The build-up factor decreases with an increase in the material density at any depth penetration for energies of 1.5 MeV and lower (Manohara et al., 2011). As beam energy increased, the dominant interaction shifted to Compton scattering, which is less influenced by material density. The low-density tissues, such as the brain's white or grey matter, received a higher dose compared to bones. Despite this, high-density areas, including the cochlea—a site sensitive post-chemotherapy—still received dose deposition. The build-up factor was higher in low atomic number materials such as white and grey matter, particularly at higher energy levels where Compton scattering predominated. The dose

to soft bone containing red marrow cells remained relatively unchanged with energy increases, as its density is not distinctly visible in medical CT and remains unconsidered in dose calculations. These results can serve as a basis for integrating different modalities, such as VMAT and Gamma Knife, in radiotherapy treatment planning.

6. Conclusion

The study of dose distribution behaviour in micro-level heterogeneous areas can enhance the development of treatment plans that reduce toxicity levels in the inner ear and cochlea. Utilising micro-CT data allows for the distinction between normal tissue, soft bone, and hard bone, unlike medical CTs that only differentiate between normal tissue and hard bone. Soft bone, which contains cells sensitive to radiation damage, is crucial in treatment planning. In low energy beams, the photoelectric effect does not significantly increase the dose to soft bone, with most of the dose being deposited in high-density bone. However, the contribution of low energy to the overall dose is minor compared to that of high energy beams. This nuanced understanding of dose deposition can lead to more precise and safer radiation therapy strategies, particularly in regions with delicate structures such as the cochlea.

References

Barrett, J.F., Keat, N., 2004. Artifacts in CT: Recognition and Avoidance. RadioGraphics 24, 1679–1691. https://doi.org/10.1148/rg.246045065

Green, D.E., Rubin, C.T., 2014. Consequences of irradiation on bone and marrow phenotypes, and its relation to disruption of hematopoietic precursors. Bone 0, 87–94. https://doi.org/10.1016/j.bone.2014.02.018

Kry, S.F., Feygelman, V., Balter, P., Knöös, T., Charlie Ma, C.-M., Snyder, M., Tonner, B., Vassiliev, O.N., 2020. AAPM Task Group 329: Reference dose specification for dose calculations: Dose-to-water or dose-to-muscle? Med. Phys. 47, e52–e64. https://doi.org/10.1002/mp.13995

Lee, B., Cho, S., Park, H.C., Kang, S.-W., Kim, J.-S., Chung, J.-B., 2022. Assessment of dose perturbations for metal stent in photon and proton radiotherapy plans for hepatocellular carcinoma. Radiat. Oncol. (Lond. Engl.) 17, 125. https://doi.org/10.1186/s13014-022-02100-8

Lee, H., Yoon, J., Park, K., Rim, C.H., Chung, M.J., Seong, J., 2019. Dose perturbation by metallic biliary stent in external beam radiotherapy of pancreato-biliary cancers. Australas. Phys. Eng. Sci. Med. 42, 745–756. https://doi.org/10.1007/s13246-019-00774-1

Manohara, S.R., Hanagodimath, S.M., Gerward, L., 2011. Energy absorption buildup factors of human organs and tissues at energies and penetration depths relevant for radiotherapy and diagnostics. J. Appl. Clin. Med. Phys. 12, 296–312. https://doi.org/10.1120/jacmp.v12i4.3557

Muñoz-Montplet, C., Marruecos, J., Buxó, M., Jurado-Bruggeman, D., Romera-Martínez, I., Bueno, M., Vilanova, J.C., 2018. Dosimetric impact of Acuros XB dose-to-water and dose-to-medium reporting modes on VMAT planning for head and neck cancer. Phys. Med. 55, 107–115. https://doi.org/10.1016/j.ejmp.2018.10.024

Radojčić, Đ.S., Kolacio, M.Š., Radojčić, M., Rajlić, D., Casar, B., Faj, D., Jurković, S., 2018. Comparison of calculated dose distributions reported as dose-to-water and dose-to-medium for intensity-modulated radiotherapy of nasopharyngeal cancer patients. Med. Dosim. 43, 363–369. https://doi.org/10.1016/j.meddos.2017.11.008

X-Ray Mass Attenuation Coefficients, 2009. NIST. https://www.nist.gov/pml/x-ray-mass-attenuation-coefficients

Yin, Z., Hugtenburg, R.P., Beddoe, A.H., 2002. Response of silicon diode dosemeters to scattered radiation from megavoltage photon beams. Radiat. Prot. Dosim. 101, 415–418. https://doi.org/10.1093/oxfordjournals.rpd.a006014